

High-Concentration Additive and Triiodide/Iodide Redox Couple Stabilize Lithium Metal Anode and Rejuvenate the Inactive Lithium in Carbonate-Based Electrolyte

Zuxin Wen, Wenqiang Fang, Xiaoyu Wu, Zuoyu Qin, Hong Kang, Long Chen, Ning Zhang, Xiaohe Liu, and Gen Chen*

Carbonate-based electrolytes are incompatible with lithium (Li) metal anode because the generated solid electrolyte interphase (SEI) undergoes repeated breakage-repair, resulting in the accumulation of inactive Li including Li^+ compounds and electrically isolated dead Li^0 in the SEI. Therefore, exploiting a suitable strategy to construct a stable SEI while efficiently rejuvenating the inactive Li capacity is urgent and more thoughtful than just building a stereotyped SEI layer. Herein, an innovative strategy is proposed of high-concentration additive (HCA) of LiNO_3 inspired by (localized) high-concentration electrolyte and inactive Li restoration methodology via triiodide/iodide (I_3^-/I^-) redox couple to improve the compatibility of carbonate-based electrolytes. The HCA of LiNO_3 can maintain the cation-anion aggregates solvation structures in the carbonate-based bulk electrolyte and induce the *in situ* formation of superior-ionic-conductivity NO_3^- -derived SEI. Moreover, the reversible I_3^-/I^- redox couple can further optimize the SEI and constantly rejuvenate the inactive Li including solvent/ LiNO_3 -derived Li_2O , a derivative has almost been acquiescent in LiNO_3 -additive electrolytes, and dead Li^0 into delithiated cathode. Consequently, epitaxy-like planar Li deposition, better reversibility, and higher capacity retention can be realized and are systematically verified by $\text{Li}||\text{Cu}$ half cells, full cells with excess/limited Li (N/P ratio = 1.5) and anode-free lithium metal batteries.

1. Introduction

Metallic lithium (Li) has long been regarded as the ultimate alternative for intercalation-limited graphite anode that has approached its theoretical capacity (372 mAh g⁻¹).^[1]

Z. Wen, W. Fang, Z. Qin, H. Kang, L. Chen, N. Zhang, G. Chen
 School of Materials Science and Engineering
 Central South University
 Changsha, Hunan 410083, P. R. China

E-mail: geenchen@csu.edu.cn

X. Wu
 Department of Chemistry
 Southern University of Science and Technology
 Shenzhen, Guangdong 518055, P. R. China

X. Liu
 School of Chemical Engineering
 Zhengzhou University
 Zhengzhou, Henan 450001, P. R. China

 The ORCID identification number(s) for the author(s) of this article can be found under <https://doi.org/10.1002/adfm.202204768>.

DOI: 10.1002/adfm.202204768

because of its highest theoretical capacity (3860 mAh g⁻¹), lowest redox potential (~3.04 V vs standard hydrogen electrode) and modest density (0.534 g cm⁻³).^[2] However, the commercial carbonate-based electrolytes such as ethylene carbonate (EC)-centric electrolyte used in graphite-based Li-ion battery are incompatible with Li anode due to the heterogeneous and brittle solid electrolyte interphase (SEI) derived from carbonate solvents,^[3] which not only exacerbates Li dendrite growth and electrolyte consumption but also devastates the Coulombic efficiency (CE) and lifespan of rechargeable Li metal battery (LMB).^[4] Moreover, repeated breakage-repair of SEI and Li dendrite growth cooperatively facilitate the formation of inactive Li, including Li^+ -containing compounds in the SEI and dead metallic Li^0 encapsulated by insulating compounds of SEI such as Li_2O , Li_2CO_3 and so on.^[5] And very recent researches have identified the dead Li^0 instead of SEI compounds as the dominant source of capacity decay.^[6]

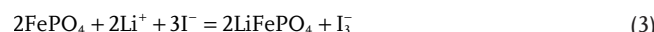
In contrast, ether-based electrolytes have

remarkably superior compatibility than carbonate-based electrolytes due to the formation of flexible organic oligomers.^[7] However, the low interfacial energy and strong binding affinity between organic SEI and Li surface limit its role in inhibiting infinite volume change during Li plating/stripping.^[8] Lithium nitrate (LiNO_3), an almost indispensable additive in ether-based electrolyte, can effectively passivate the Li surface through NO_3^- -derived inorganic-rich SEI.^[9] The *in situ* generated nitrides/nitrogen oxides (such as Li_3N , LiNO_2 , etc.) present high interfacial energy, Young's modulus and Li-ion conductivity, which boost the lateral growth of Li deposition and significantly restrain the dendrite growth and the derivation of dead Li^0 .^[10] In spite of superior compatibility against metallic Li, LiNO_3 -modified ether-based electrolytes are still not appreciated due to their limited oxidative stability (<4 V) and conventional carbonate-based electrolytes (~4.3 V) are still prospective candidates for high-voltage battery in short-term future.^[11] Although considered to be the one of the most successful additive in ether-based electrolyte, the application of LiNO_3 in carbonate-based electrolyte has been shelved frequently due to low solubility (~0.01 mg mL⁻¹).

Extensive work has been devoted to the solubilization of LiNO_3 in carbonate-based electrolyte. The most straightforward method is to construct ether-carbonate cosolvent electrolyte where LiNO_3 can be used as additive or Li salt; while this method narrows the electrochemical window inherent in carbonate-based electrolyte.^[12] Besides, some solvents with high Gutmann donor number (DN) and salts with Lewis acid sites, mainly including dimethyl sulfoxide,^[13] sulfolane,^[11a] γ -butyrolactone,^[14] tris(pentafluorophenyl)borane,^[15] copper fluoride,^[16] tin trifluoromethanesulfonate,^[17] can work as solubilizers. On the one hand, these solubilizers can indeed solubilize LiNO_3 and improve the cycling performance of carbonate-based electrolyte remarkably. On the other hand, solubilizers with high DN and Lewis acid sites intrinsically react violently with Li^[18] and have stronger coordination capability with cations, which decoordinate the NO_3^- from solvation shell of cation and impede the access into electric double layer leading to weakened utility of NO_3^- .^[19] Moreover, the electrolytes used in the above-mentioned work are usually fluoroethylene carbonate (FEC)-based, an high-efficiency additive in carbonate-based electrolyte,^[20] rather than the most common EC-based electrolyte, which may greatly obscure the role of LiNO_3 (detailed compositions are shown in Table S1 in the Supporting Information). Therefore, there is an urgent need to exploit a Li-compatible LiNO_3 solubilizer used in conventional EC-based electrolytes without sacrificing the merits of carbonate-based electrolytes.

Inspired by (localized) high-concentration electrolyte ((L)HCE) where free solvent molecules sharply reduce and contact ion pairs (CIPs) and cation–anion aggregates (AGGs) generate, leading to enhanced oxidation stability and anion-tuned SEI,^[21] we herein proposed the idea of high-concentration additive (HCA), that is, adding the high-concentration LiNO_3 solution into carbonate-based electrolyte with additive-level content. Li-compatible tetraglyme (G4) was employed as solubilizer due to its proper DN, abundant solvation sites, higher solubility of LiNO_3 , oxidation stability (≈ 4 V) than conventional ether solvents (such as DME, DOL).^[22] It is demonstrated that the CIPs and AGGs can be achieved when HCA of LiNO_3 is added to carbonate-based electrolytes which can be considered as diluent in LHCE due to the feeble solubility to LiNO_3 . Furthermore, triiodide/iodide (I_3^-/I^-) redox couple were also introduced. Previous work about $\text{Li}-\text{O}_2$ batteries^[23] has demonstrated that the coexistence of halogen ions and NO_3^- can induce dendrite-free epitaxial growth of Li metal, which is recommended by extensive literature due to minimized microstructural tortuosity and mitigation of electrically isolated dead Li^0 .^[5,17] Halogen ions can permeate and destroy the original SEI layer, prompting stripping of the incompact original passivation layer and reducing the thickness of the passivation layer. NO_3^- ions can immediately passivate the freshly exposed Li metal surface by forming nitride/oxide-rich, compact and thin SEI layer. Moreover, the I_3^-/I^- redox couple not only play an important role in optimizing the SEI in Li anode but also as a redox mediator in reclaiming inactive Li capacity into delithiated cathode. I_3^- can spontaneously rejuvenate the irreversible Li capacity in Li_2O and dead Li^0 debris electrically isolated by insulating SEI components through chemical reactions (Equations (1) and (2)).^[24] And the generated I^- can be chemically oxidized back to I_3^- by delithiated cathode (such as iron phosphate, FePO_4 , Equation (3)) or

electrochemically oxidized when the working voltage of cathode exceeds 2.9 V.^[25] Moreover, the LiNO_3 -derived inferior-ionic-conductor Li_2O , an unescapable reduction product that has previously been acquiescent and neglected in LiNO_3 -additive electrolytes, can be indiscriminately eliminated by the redox couple and a nitride-dominated SEI can be obtained artfully. Systematic experimental characterizations, phase field simulations and chemical theory calculations were used to detect the composition and nanostructure and interpret the emerging electrochemical phenomena.



Consequently, the carbonate-based electrolyte with HCA of LiNO_3 and I_3^-/I^- redox couple significantly optimizes the Li plating morphology and enhances the Li^+ transfer kinetics. The $\text{Li}||\text{Cu}$ half cells with designed electrolyte delivered high average CE of 98.27% for over 200 cycles at 0.5 mA cm⁻² with fixed discharging capacity of 1.0 mAh cm⁻². LMBs with lithium iron phosphate (LiFePO_4 , LFPO, 12 mg cm⁻²) exhibit high discharge capacity retention rate (88.4%) for 500 cycles at 1 C (1 C = 170 mAh g⁻¹) and 93.3% with lithium–nickel–cobalt–manganese oxide ($\text{LiNi}_{0.5}\text{Co}_{0.2}\text{Mn}_{0.3}$, NCM523, 12 mg cm⁻²) at 0.5 C (1 C = 200 mAh g⁻¹) for 100 cycles. Moreover, both LMBs at extremely low negative to positive areal capacity ratio (N/P, 1.5) and anode-free lithium metal battery (AFLMB) alleviate the decay of discharge capacity, confirming the utility of I_3^-/I^- redox couple in reclaiming inactive Li.

2. Results and Discussions

The conventional carbonate-based electrolyte (LP30) with 1 M LiPF_6 dissolved in EC-dimethyl carbonate (DMC) (1:1 by volume) was used as the basic electrolyte and 5 vt% FEC-containing LP30 (LPF) was also employed as control electrolyte. HCAs were prepared by dissolving 1, 2, 3, 4 M LiNO_3 in G4 (G4_n , n represents the concentration of LiNO_3 in G4) and HCAs of LiNO_3 can keep transparent without obvious precipitation due to the high solubility of LiNO_3 in G4 (Figure S1, Supporting Information). 5 vt% G4_n and 5 vt% FEC were added to LP30 and no obvious precipitation can be observed (Figure 1a; Figure S2a–c, Supporting Information), even when 5 vt% G4_4 was added (≈ 0.2 M LiNO_3 , LPFN). However, with the same amount of LiNO_3 (0.2 M) in LP30 and LPF, LiNO_3 particles hardly dissolves in both two electrolytes (Figure S2d,e, Supporting Information). To introduce the I_3^-/I^- redox couple into carbonate-based electrolyte, 0.01×10^{-3} M I_2 was added to LPFN (denoted as LPFN-i₂) to reclaim the inactive Li capacity in solvent/ LiNO_3 -derived Li_2O and dead Li^0 . With the addition of I_2 , the color evolution from colorless to reddish-brown will emerge (Figure 1b; Figure S3, Supporting Information) and significantly enhanced flame retardancy will be obtained unexpectedly due to the presence of halogen (Figure S4,

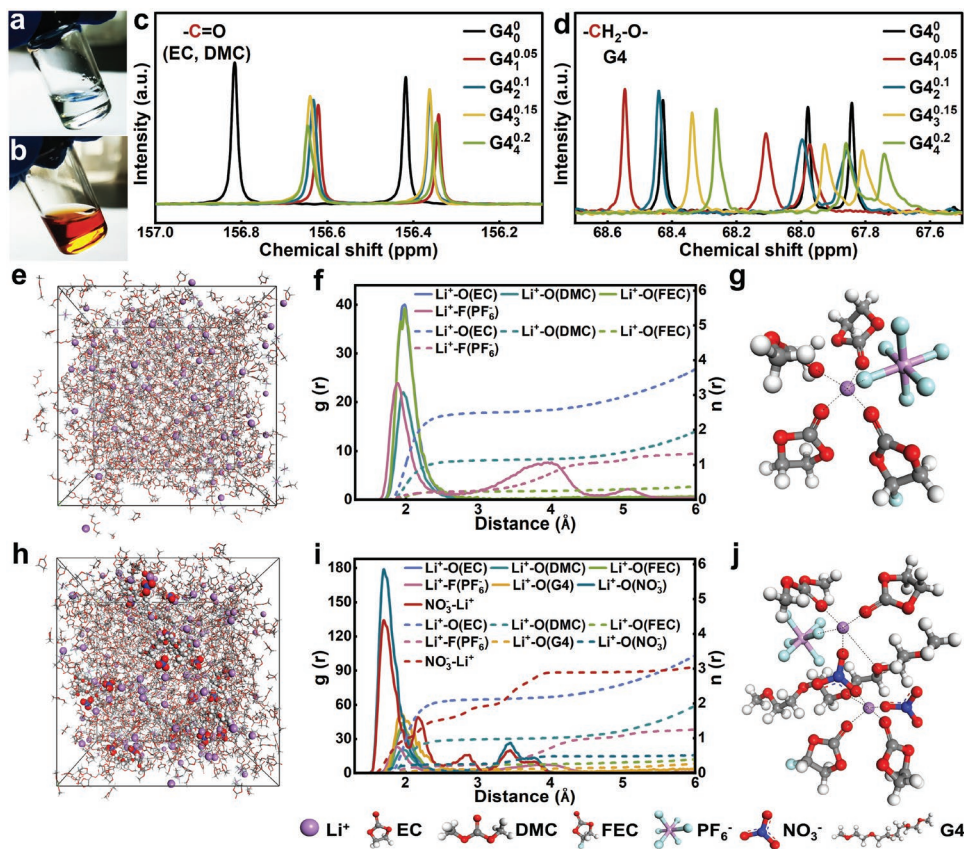


Figure 1. The characterization and MD simulation of Li^+ -solvation structure. The digital photographs of a) LPFN and b) LPFN-i₂. ¹³C NMR spectra of c) the carbonyl carbon in EC and DMC and d) the methylene carbon in G4. e–g) and h–j) Represent the MD simulation of the controlled electrolyte LPF and the additive-containing LPFN-i₂, respectively. e,h) The snapshot of the constructed amorphous cell after dynamic simulation for 40 ps. f,i) The RDF ($g(r)$, solid lines) and coordination numbers ($n(r)$, short dash lines). g,j) Schematic diagram of representative Li^+ -solvation structure.

Supporting Information).^[25b] In addition, the amount of I_2 should be strictly controlled to prevent the further pitting corrosion on active Li according to the previous literature.^[23,26]

To explore the effect of additives on solvation structure, nuclear magnetic resonance (NMR) was employed. A series of LPFN-i₂ type electrolytes with 5 v/v% varied G4_n were prepared (denoted as G4_n, n,m represents the concentration of LiNO_3 in G4 and in bulk electrolyte respectively. G4₀ refers to the addition of 5 v/v% pure solvent of G4 and G4_{0.2} is LPFN-i₂ mentioned above. Detailed preparation of G4_n can refer the Supporting Information). The chemical shifts shown in ¹³C NMR spectra of carbonate solvents/additive (EC, DMC, and FEC) are completely different from that of G4. When 0.05 M LiNO_3 is present in the bulk electrolyte (G4_{1.05}), the ¹³C spectra of carbonyl carbon atom in EC and DMC shift up-filed to a lower chemical shift while down-filed to a higher chemical shift for methylene carbon atom in G4 (Figure 1c,d). For such opposite chemical shifts, it is deduced that part of electron-rich^[27] NO_3^- ions enter the Li^+ solvation shell originally dominated by carbonate molecules (EC, DMC, and FEC), which donates negative charge and strong shielding effect to carbonate molecules but deshielding effect to G4 due to the escape of NO_3^- and solvation of Li^+ . However, the chemical shift values of carbonyl carbon atom in EC and DMC remain almost constant. There are no obvious great up-field shifts as the further increment of LiNO_3 concentration

(Figure 1c). In contrast, the continuously decreasing chemical shift values indicates the density of electron cloud surrounding the G4 molecules increases (Figure 1d). The bizarre phenomenon may be attributed to the very limited solvation capability of carbonate molecules for LiNO_3 . And the excess LiNO_3 beyond the solubility limit of carbonate-based electrolyte is mainly solvated by high-DN G4 molecules. As the concentration of LiNO_3 increases, the free G4 molecules are remarkably decreasing and NO_3^- ions need to participate in the Li^+ solvation sheath to maintain electrical neutrality. Furthermore, the other ¹³C spectra features associated with FEC and EC and ¹H spectra of G4_n show the analogous chemical shift pattern as above (Figures S5 and S6, Supporting Information). Meanwhile, the Raman spectra of G4_n and G4_m were also carried out to further study the solvation structure. The typical O–C–O bending and bands^[28] of G4 solvent at 770–870 cm⁻¹ are maintained in the spectrogram. Nevertheless, they become much weaker and shift to higher value as gradually increasing LiNO_3 concentration (Figure S7, Supporting Information), which implies that G4 molecules are coordinated with Li^+ to form $[\text{Li}(G4)]^+$ complexes and leads to a sharp concentration drop of free G4 molecules. The peaks located at 1040 cm⁻¹ refer to the symmetric stretch^[14] of free NO_3^- and the shoulder peaks at higher value emerge and dominate with increasing concentration (Figure S7, Supporting Information), indicating NO_3^- ions enter the solvation

shell to form CIPs and AGGs in HCAs. The analogous trends of O–C–O bend and NO_3^- symmetric stretch are also detected in $\text{G}4_n^m$ (Figure S8a,b, Supporting Information). No obvious deviations of the O–C–O bending bands of EC and FEC at 700–750 cm^{-1} can be observed with the increasing LiNO_3 concentration (Figure S8c, Supporting Information), further confirming NO_3^- ions coordinate with $[\text{Li}(\text{G}4)]^+$ complexes and the aggregates structure can be well reserved even though additive-level high-concentration $\text{G}4_n$ is added into the carbonate-based bulk electrolyte. It is worth noting that such an experimental phenomenon is similar to LHCE and the carbonate solvents (EC, DMC, and FEC) are equivalent to diluents in LHCE due to their very limited solubility to LiNO_3 compared to G4.

Molecular dynamic (MD) was employed to elucidate the effect of additives on solvation structure on molecular scale. The carbonate solvent molecules (EC and DMC) dominate the first Li^+ -solvation sheath in conventional LP30 (Figure S9, Supporting Information), resulting in carbonate-derived organic SEI. However, FEC-added LPF appears an obvious Li^+ -O(FEC) peak at around 1.98 Å in the radial distribution function (RDF), indicating the participation of FEC in solvation structure (Figure 1e–g). To investigate the solvation behavior of HCA of LiNO_3 in carbonate-based bulk electrolyte, a series of MD simulations of $\text{G}4_n^m$ electrolytes were conducted. In order to reduce the computational difficulty and provide accurate understanding of the role of NO_3^- , we consider the effect of I_2 on solvation structure is minimal, since the content of I_2 (0.01×10^{-3} M) is several orders of magnitude less than that of LiNO_3 . An intense peak assigned to Li^+ -O(NO_3^-) emerges in RDF at around 1.70 Å and the coordination number for NO_3^- increases from 0.017 ($\text{G}4_1^{0.05}$) to 0.252 ($\text{G}4_4^{0.2}$) with the concentration augment of HCA (Figure 1h–j; Figure S10, Supporting Information), indicating that the NO_3^- is involved in the primary solvation sheath and inorganic-containing SEI derived from NO_3^- becomes feasible. Moreover, the G4 continuously enter the Li^+ solvation sheath (≈ 2.0 Å) and the free G4 molecules are decreasing dramatically to dissolve the excess LiNO_3 that exceeds the solubility limit of the carbonate electrolyte (Figures S10 and S11, Supporting Information). Interestingly, each NO_3^- will coordinate with 1.02 Li^+ ion in $\text{G}4_3^{0.15}$ and 1.55 in $\text{G}4_4^{0.2}$ (namely, LPFN-i₂), which is greater than 1 and indicates the formation of local cation–anion aggregates structure^[13] (Figure S11, Supporting Information). In addition, the resemblant aggregation structure and coordination environment trend of NO_3^- and G4 can also be observed in HCA of LiNO_3 (namely, $\text{G}4_n$, Figures S12 and S13, Supporting Information). Combining the results of experimental characterizations and MD simulations, we can deduce that the cation–anion aggregates structure can be well maintained when HCA of LiNO_3 is added into the carbonate-based electrolyte, which is similar to the solvation structure in LHCE.

The electrochemical tests of $\text{Li}||\text{Cu}$ half cells and $\text{Li}||\text{Li}$ symmetrical cells were conducted to examine the effect of additives on long-term reversibility. As shown in Figure 2a, the CE of conventional carbonate-based electrolyte (LP30) experiences a sharp decline, begins at only 30 cycles, from 88.22% to less than 50% after only 70 cycles. Although the addition of 5 vt% FEC in LP30 (LPF) can improve the CE to some extent ($\approx 95.66\%$ within 40 cycles), severe fluctuations emerge afterwards, indicating the violent side reaction and limited effectiveness with

additive-level FEC.^[29] In contrast, much higher average CE and better reversibility ($\approx 98.10\%$ within 130 cycles for LPFN and $\approx 98.27\%$ within 200 cycles for LPFN-i₂) are achieved with the addition of HCA of LiNO_3 and I_3^-/I^- redox couple, preliminarily confirming the feasibility of HCA of LiNO_3 and the positive synergistic effect between LiNO_3 and I_3^-/I^- redox couple. Symmetric cells tests using LPFN and LPFN-i₂ present smaller overpotentials (76 vs 41 mV after 300 h), which is comparable to ether-based electrolytes.^[10a] However, ever-increasing overpotentials, fatal short circuit, and drastic fluctuations arise obviously in LP30 and LPF (Figure 2b), indicating the continuous side reactions and the accumulation of fragile SEI by-products at the Li/electrolyte interface (Figure S14, Supporting Information). The gradually decreasing nucleation overpotentials and charge transfer resistances further corroborate the improved SEI stability and faster Li^+ -transfer kinetics with the addition of LiNO_3 and I_3^-/I^- redox couple (Figure 2c,d; Figure S15, Supporting Information). Note that LPFN-i₂ can further reduce the interfacial impedance compared to LPFN, which can be ascribed to the scavenging effect of I_3^- on poor-ionic-conductor Li_2O through Equation (1) and more detailed discussion will be presented below. Cyclic voltammetry (CV) tests scanning from 2.2 to 0.0 V at 0.1 mV s⁻¹ are employed to probe the reduction reactions and corresponding potentials. Compared to LP30 and LPF, analogous reduction curves and distinct reduction peaks which can be assigned to the decomposition of LiNO_3 around 1.6 V can obtain in LPFN and LPFN-i₂ (Figure 2e). The addition of I_2 does not introduce additional reduction peak in CV because the reaction between I_3^- and Li_2O (Equation (1)) is essentially spontaneous chemical reaction. To evaluate the electrochemical oxidation window of electrolytes, linear sweep voltammetry (LSV) is conducted on stainless steel work electrode and Li foil is used as reference electrode and counter electrode. The electrochemical stability voltages of LPFN and LPFN-i₂ (≈ 4.5 V, Figure 2f) are not reduced due to the introduction of HCA and even slightly higher than LP30 (≈ 4.35 V) and LPF (≈ 4.29 V) (Figure S16, Supporting Information). Note that compared to LPFN, LPFN-i₂ exists a small oxidation peak starting at 3.6 V, which can be attributed to the electrochemical oxidation reaction^[25b] of I^- to I_3^- . However, the addition of only 5 vt% pure ether solvent into carbonate-base electrolyte (LP30 + 5 vt% pure G4) greatly destroys the oxidation stability. Surprisingly, the oxidation window becomes broader with the increase of LiNO_3 concentration (Figure S17a, Supporting Information). The same trend can also be found in a series of $\text{G}4_n$ electrolytes (Figure S17b, Supporting Information), which indirectly certifies that HCA in the bulk electrolyte can maintain the aggregated structure and the lack of free ether molecules. Moreover, the contact angles, viscosity and ionic conductivity were also provided. The contact angle, ionic conductivity and viscosity are just slightly changed after introducing the high-concentration additive and I_3^-/I^- redox couple into the conventional carbonate-based electrolytes. In sharp contrast, great increase in viscosity and sharp decrease in ionic conductivity are observed in high-concentration electrolyte ($\text{G}4_4$), indicating the strategy of high-concentration additive can effectively avoid some shortcomings (such as low ionic conductivity, high viscosity) caused by high-concentration electrolytes (Figures S18 and S19, Supporting Information). Scanning electron microscopy (SEM) is

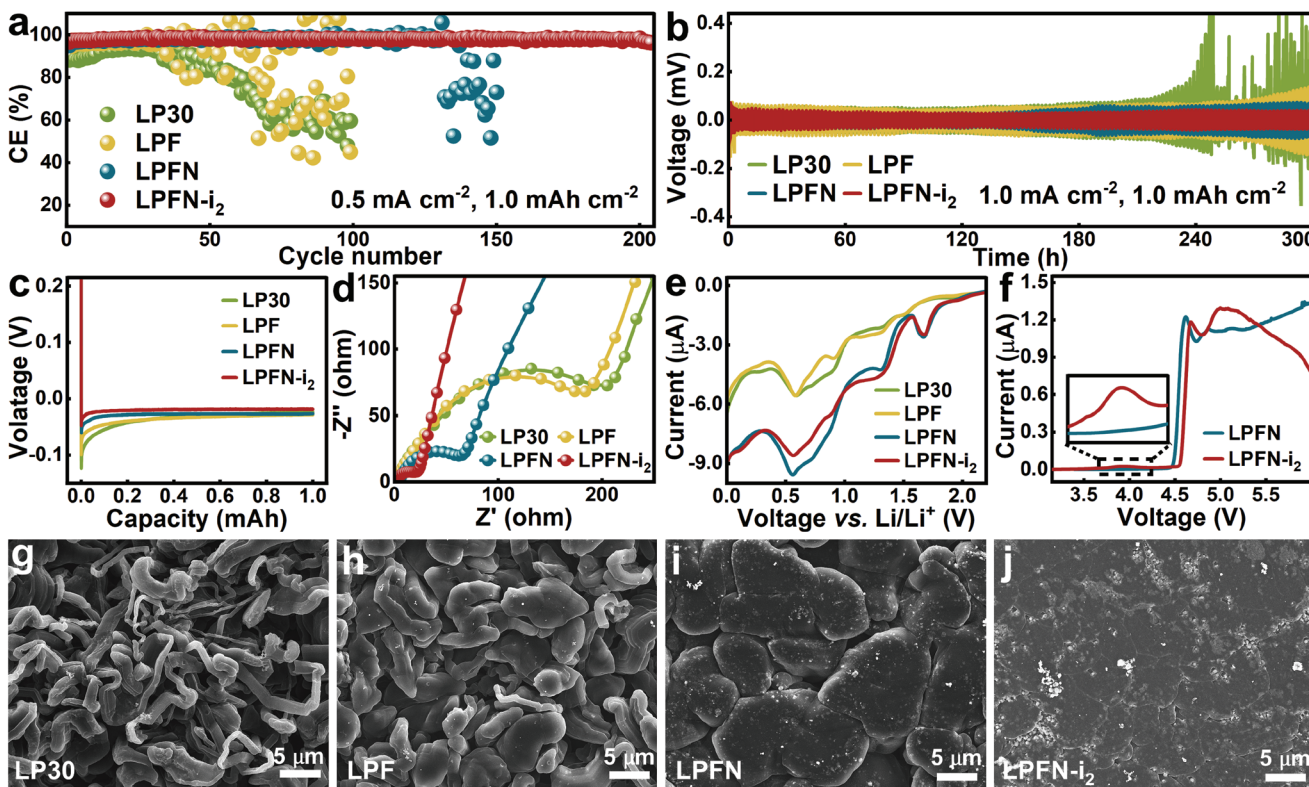


Figure 2. Electrochemical performance and Li deposition morphologies in different electrolytes. a) CEs of Li||Cu half cells at 0.5 mA cm^{-2} with fixed discharging capacity of 1.0 mAh cm^{-2} . b) Voltage–time profiles of Li||Li symmetrical cells at 1.0 mA cm^{-2} for 1.0 h in each half cycle. c) Voltage–capacity profiles of Li deposition on Cu foil at 0.5 mA cm^{-2} . d) Electrochemical impedance Nyquist spectra of Li||Cu half cells after the activation process at 0.05 mA cm^{-2} . e) CV curves of Li||Cu half cells between a voltage range of $0\text{--}2.2 \text{ V}$ at 0.1 mV s^{-1} . f) LSV curves of Li||SS cells scanned between open circuit voltage and 6 V at 0.5 mV s^{-1} . The SEM morphologies of 2.0 mAh cm^{-2} Li deposited on Cu foil at 0.5 mA cm^{-2} in g) LP30, h) LPF, i) LPFN, j) LPFN-i₂.

employed to characterize the morphologies of Li depositions after 0.1 or 2.0 mAh cm^{-2} Li plated on copper (Cu) current collector at 0.5 mA cm^{-2} . Loose and porous dendritic structures are observed in both LP30 and LPF. The morphologies with such high specific surface area will lead to continuous breakage-repair of SEI and the hazard of short circuit (Figure 2g,h; Figure S20a,b,e,f, Supporting Information). In contrast, typical dough-like and dendrite-free Li depositions with colossal granular size can be obtained in LiNO₃-containing LPFN (Figure 2i; Figure S20c,h, Supporting Information). Compared to LPFN, more planar Li deposition morphology similar to epitaxial growth is emerged in LPFN-i₂ (Figure 2j; Figure S20d,g, Supporting Information), indicating the addition of I₂ can substantially uniformize the SEI and similar results have also been reported in previous literature using other halogens in Li-air battery.^[23]

The in-depth chemical components of the SEI forming in the specific electrolytes are characterized by in-depth X-ray photo-electron spectroscopy (XPS) sputtered by Ar-ion. The indicative C 1s spectra in carbonate-based electrolyte display four binding states at 284.80, 286.01, 288.17, 289.41 eV, corresponding to C–C/C–H, C–O, C=O and Li₂CO₃ groups respectively.^[13] Compared to LP30 and LPF, the intensity of metastable organics (C–C/C–H, C–O, and C=O) derived from the decomposition of carbonate solvents are much weaker in LPFN-i₂ (Figure 3a,b; Figure S21a, Supporting Information). The trend is not obvious at the surface (0 s of etching), but distinct intensity attenuation

emerges during the rest of sputtering in LPFN (Figure S21b, Supporting Information). Moreover, the proportion of Li₂CO₃, an extremely stable SEI component with low oxidation state,^[30] gradually increases in LPFN and LPFN-i₂ while the intense C–C/C–H group always dominant the C 1s components in LP30 and LPF, indicating the organic-rich SEI and irrepressible solvent decomposition in conventional carbonate-based electrolytes (LP30 and LPF). For F 1s spectra, typical LiF signal at 684.44 eV is observed in these four electrolytes. Obviously, the LiF is mainly derived from the reduce of LiPF₆ in FEC-absent LP30. However, the sacrificial-additive FEC will replace LiPF₆ as the main decomposition source of LiF in other three FEC-containing electrolytes,^[31] which will be further discussed by theoretical calculation in the following section. It is demonstrated that the LiF signal intensity improves significantly as the sputtering deepens in LP30, LPF, and LPFN, revealing LiF-rich inner SEI. However, for LPFN-i₂, the content of LiF in the SEI is more uniform and the intensity is much smaller than that of the other electrolytes. For LiNO₃-containing electrolytes (LPFN and LPFN-i₂), an additional Li₃N peak at 298.45 eV emerges in the SEI, confirming the reduction of LiNO₃ in carbonate-based electrolyte. By contrast with LiF, Li₃N not only possesses excellent electronic insulation and interfacial energy but also much smaller Li⁺ diffusion energy barrier (0.007 vs 0.729 eV).^[32] It endows Li₃N with super ionic conductivity ($\approx 10^{-3} \text{ S cm}^{-1}$ at room temperature, comparable to that of liquid electrolyte)^[33]

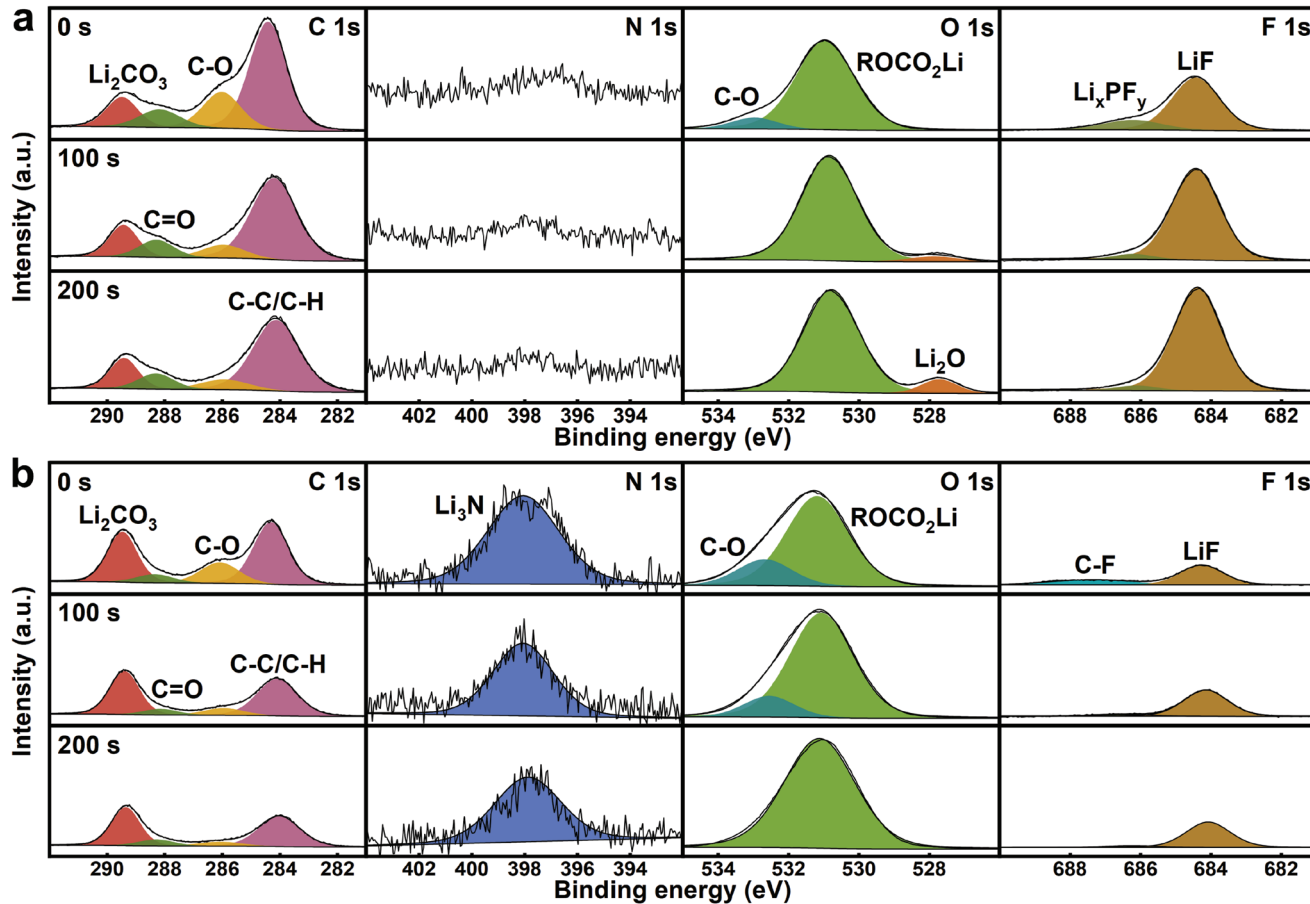


Figure 3. The in-depth XPS spectra of Li metal surface after 12 cycles of plating in Li||Li symmetric cells at 1.0 mA cm⁻² with 1.0 mAh cm⁻² fixed capacity in a) LPF and LPFN-i₂.

and induces planar and dense Li deposition,^[34] as seen in the results of SEM (Figure 2i,j). For O 1s spectra, the ROCO₂Li at 530.97 eV dominate the content in these four electrolytes, which is consistent with previous literature using carbonate-based electrolyte.^[16,35] However, comparatively higher C–O group content at 532.97 eV is found in LPFN-i₂ than that of the other electrolytes and is still clearly visible even after 100 s of sputtering (Figure 3b; Figure S22, Supporting Information), which can be attributed to the catalytic effect of I⁻ in promoting the H-abstraction reaction of solvent molecules to form elastic and Li⁺-conductive oligoether.^[36] In addition, no obvious Li₂O signal emerges at 527.72 eV, further affirming the scavenging effect of I₃⁻ on Li₂O. Unexpectedly, the Li₂O content in the innermost SEI reaches up to 17.3% in LPFN, far exceeding that in LP30 (10.0%) and LPF (8.1%) (Figure S22, Supporting Information). The reason for improved Li₂O content is promoted by the decomposition of LiNO₃ and have been verified in previous literature using LiNO₃ as additive in carbonate-based electrolyte.^[10b,13,15,37] Therefore, the addition of LiNO₃ into electrolyte not only introduces fast-ionic-conductor Li₃N but also interior-ionic-conductor Li₂O into SEI. The influence of Li₂O on deposition morphology will be detailedly discussed below, which is commonly neglected in previous researches using LiNO₃ as additive. In addition to the XPS spectra of the above elements, I

3d spectra are specially conducted for Li surface in LPFN-i₂ and no obvious peaks are detected (Figure S23, Supporting Information), which can be ascribed to the high solubility of iodide in aprotic liquid electrolyte^[38] and indirectly proves the interconversion between iodides in bulk electrolyte.

Cryogenic transmission electron microscopy (cryo-TEM) was further used to visualize the nanostructure and components distribution of the SEIs generated in different electrolytes. In the basic carbonate electrolyte without any additives (LP30), typical mosaic structure filled with diverse Li⁺ SEI components (including Li₂O, LiF, Li₂CO₃) and nubby dead Li⁰ surrounded by these electrically insulating Li⁺ components are discovered, confirming by the corresponding fast Fourier transform (FFT) patterns and lattice fringes patterns (Figure 4a). However, LiF dominates and passivates the SEI in FEC-added LPF electrolyte due to the sacrificial decomposition of FEC. Although the addition of FEC can passivate and improve the SEI to some extent, dead Li⁰ can still be clearly detected (Figure 2b), which may be ascribed to the huge volume effect brought by Li dendrite growth. The resulting irreversible capacity loss also determines that the improved CE is still not enough to achieve long cycling lifespan in LPF with FEC as additive instead of solvent.^[39] For LPFN with HCA of LiNO₃, the new component Li₃N derived from LiNO₃ and LiF dominate the majority

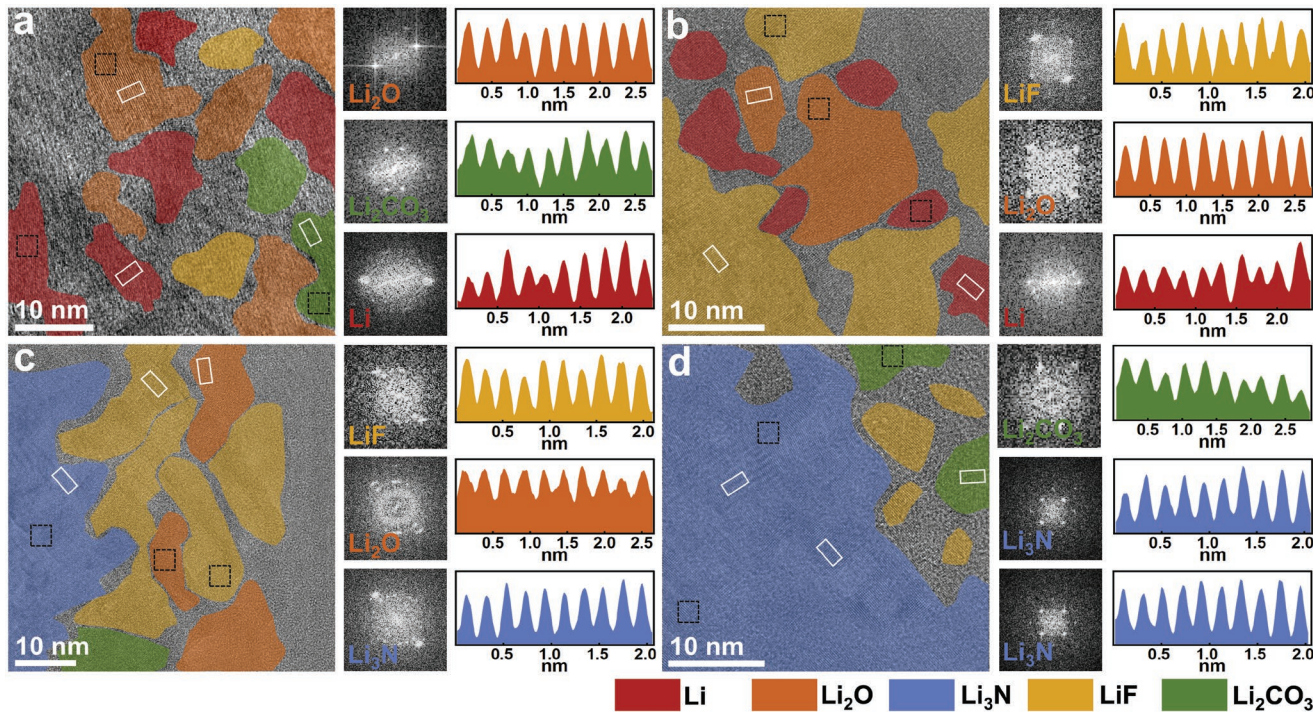


Figure 4. Nanostructures and components of SEIs generated in different electrolytes imaged by cryo-TEM. a–d) correspond to the results for LP30, LPF, LPFN, and LPFN-i₂. The FFT patterns are grabbed from the black square areas and the lattice fringes patterns from white rectangular areas marked in the high-resolution cryo-TEM images.

of the SEI and Li₂O/Li₂CO₃ chunks are randomly interleaved between Li₃N and LiF (Figure 4c). In stark contrast, only Li₃N dominate almost the entire SEI with a small amount of LiF and Li₂CO₃ scatter in LPFN-i₂ electrolyte with I₃⁻/I⁻ redox couple (Figure 4d). Consistent with the results of XPS, Li₂O and dead Li⁰ are barely detected due to the efficient scavenging of Li₂O and dead Li⁰ recovery by I₃⁻/I⁻ redox couple and much weaker plating/stripping volume effect with Li₃N-rich and homogeneous SEI. Meanwhile, compared with LPFN, LiF is also greatly reduced, indicating the inhibition of the degradation of FEC with the addition of I₃⁻/I⁻ redox couple. It is speculated that the I₃⁻/I⁻ redox couple can quickly clean the inherent passivation layer on the surface of Li foil when LPFN-i₂ is in contact with the Li foil, enabling the LiNO₃-derived Li₃N to cover the Li foil surface more comprehensively and suppressing subsequent decomposition of FEC. On basis of in-depth XPS and cryo-TEM results, a Li₃N-rich SEI with simpler compositions and more homogeneous nanostructure can be obtained in I₂-added LPFN-i₂ electrolyte.

An ex situ visualization experiment conducted by ultraviolet spectrophotometry (UV) is carried out to validate the reversibility and mechanism of I₃⁻/I⁻ redox couple. The broad peak at around 229 nm can be assigned to the absorption of I⁻ in LiI-containing DMC solution (LiI-DMC), while the characteristic peaks at 215, 288, and 360 nm emerging in I₂-containing DMC solution (I₂-DMC) belong to I₃⁻ (Figure 5a),^[24,26] the predominant form of I₂ in polar solution.^[25a,38] After adding a cycled Li (12 cycles in Li||Li symmetric cell with LP30) into the I₂-DMC solution, evident peak broadening at around 229 nm and peak intensity weakening at 288 and 360 nm are observed

in UV spectra, indicating the emergence of I⁻ and the decrease of I₃⁻ through Equations (1) and (2). The color of I₂-DMC solution will also change from reddish-brown to bright yellow at the same time. In addition, the black pristine SEI accumulation on cycled Li surface can also be removed, similar to chemical polishing,^[40] and the XRD spectra show improved Li crystallinity and reduced impurity peaks (Figure 5b). Upon the continuous addition of delithiated gray-white iron phosphate (FePO₄) into the cycled Li-reacted I₂-DMC solution, the broad peak representing I⁻ disappeared while the intensity of I₃⁻ peaks are restored (Figure 5a). However, the colour of the solution does not return to the expected reddish-brown like I₂-DMC because of the large amount of black lithiated FePO₄ suspended in the solution. XRD patterns prove the appearance of LiFePO₄ after the spontaneous lithiation of FePO₄ through Equation (3) (Figure 5c). The original reddish-brown of the LiFePO₄-containing solution will appear after centrifuging (Figure S24, Supporting Information), indicating the regeneration of I₃⁻ in this solution.

Physical field simulations and chemical calculations were synergistically carried out to further interpret the chemical/electrochemical phenomena observed above. Referring to the characterizations implemented on SEI, finite element analysis based on surface film resistance method were achieved by COMSOL Multiphysics 5.6 to elucidate the Li deposition behavior in different electrolytes matching with different SEI compositions and structures (detail model geometry construction and physics boundary condition settings can be found in the explanatory text and figures in the Supporting Information). Due to diversity and heterogeneity of SEI composition in

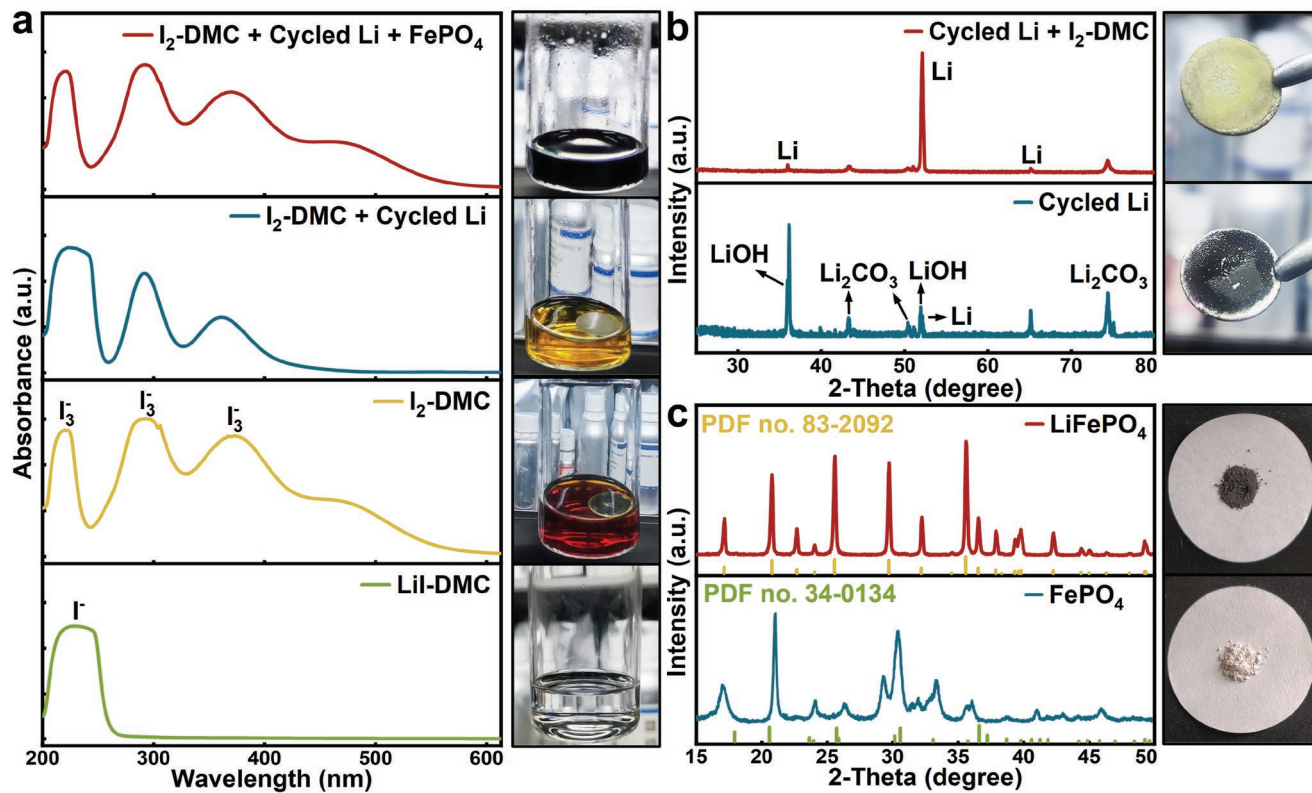


Figure 5. The intrinsic mechanism of I_3^-/I^- redox couple for rejuvenating the dead Li and scavenging Li_2O . a) UV spectra and the colour evolution of I^- -containing solution. b) XRD patterns and digital photographs of cycled Li foil and cycled Li foil soaked into I_2 -DMC solution. c) XRD patterns and digital photographs of $FePO_4$ and lithiated $FePO_4$ soaked in LiI -DMC solution.

LP30 and LPF, Li ions tend to accumulate in some hot spots, result in uneven Li nucleation and dendrites growth (Figure 6a; Figure S26, Supporting Information). Typically, high ionic conductivity regions can act as hot spots where Li^+ flux tend to transport as indicated by the streamlines rather than the surrounding low ionic conductivity regions (Figure S28, Supporting Information). In addition, the effect of electrically isolated dead Li^0 in SEI on deposition behavior is also specially considered, the dead Li^0 will distort and derange the Li^+ flux as a physical block and eventually lead to dendrite growth (Figure 6b; Figure S30, Supporting Information). For LPFN electrolyte, the simulation shows that Li grows significantly faster in high ionic conductivity Li_3N -rich regions than low ionic conductivity $Li_2O/LiF/Li_2CO_3$ -rich regions and dough-like morphology emerges over time (Figure 6c; Figure S32, Supporting Information), which is in good agreement with the images observed by SEM. In sharp contrast, due to the scavenging effect of I_3^- for solvent-derived and $LiNO_3$ -derived poor-ionic-conductor Li_2O and dead Li^0 and the reduction of LiF, the Li_3N -dominant SEI enables a more uniform Li^+ flux and concentration gradient distribution, resulting in planar and dense Li deposition in LPFN- i_2 electrolyte (Figure 6d; Figure S34, Supporting Information). Systematic chemical calculations are also performed to disclose the chemical properties of electrolyte components and the intrinsic mechanism of chemical/electrochemical reaction. In comparison with carbonate solvents (EC, DMC, and FEC), the selected solubilizer G4 has the lowest binding energy ($-276.2\text{ kJ mol}^{-1}$,

Figure 6e), in agreement with the lowest electrostatic potential (ESP) and relatively low positive charge distribution of G4 (Figure S35, Supporting Information). The lowest binding energy means stronger affinity of G4 with Li^+ than carbonate solvents, which not only endows G4 with higher $LiNO_3$ solubility but also greater tendency to reduce on the Li surface to form elastic oligoether due to the higher desolvation energy (namely, binding energy). Under the catalytic effect of I_3^- ^[36] we can also explain the higher C-O peak intensity in O 1s spectra in LPFN- i_2 compared to LPFN. The reaction energies between I_3^- and various SEI components are evaluated by density functional theory (DFT). We find that the chemical reaction between I_3^- and Li_2O (Equation (1)) or Li (Equation (2)) is energetically favorable ($\Delta E < 0\text{ kJ mol}^{-1}$, Figure 6f) but unfavorable with LiF, Li_3N , LiOH, and Li_2CO_3 ($\Delta E > 0\text{ kJ mol}^{-1}$, Figure S36, Supporting Information), suggesting that I_3^- can selectively scavenge the unfavorable components (Li_2O and dead Li^0) and retain the SEI-valid components (such as LiF and Li_3N). Moreover, the reaction to rejuvenate the irreversible Li capacity into delithiated cathode through I_3^-/I^- redox couple is exothermic (Equation (3), $\Delta E = -375.3\text{ kJ mol}^{-1}$), indicating the reaction can proceed spontaneously and ensure the regeneration of I_3^-/I^- redox couple while recovering the inactive Li capacity. The frontier molecular theory is employed to evaluate the redox reaction activity of the electrolyte components by calculate the energy level of the lowest unoccupied molecular orbital (LUMO) and the highest occupied molecular orbital (HOMO). Compared

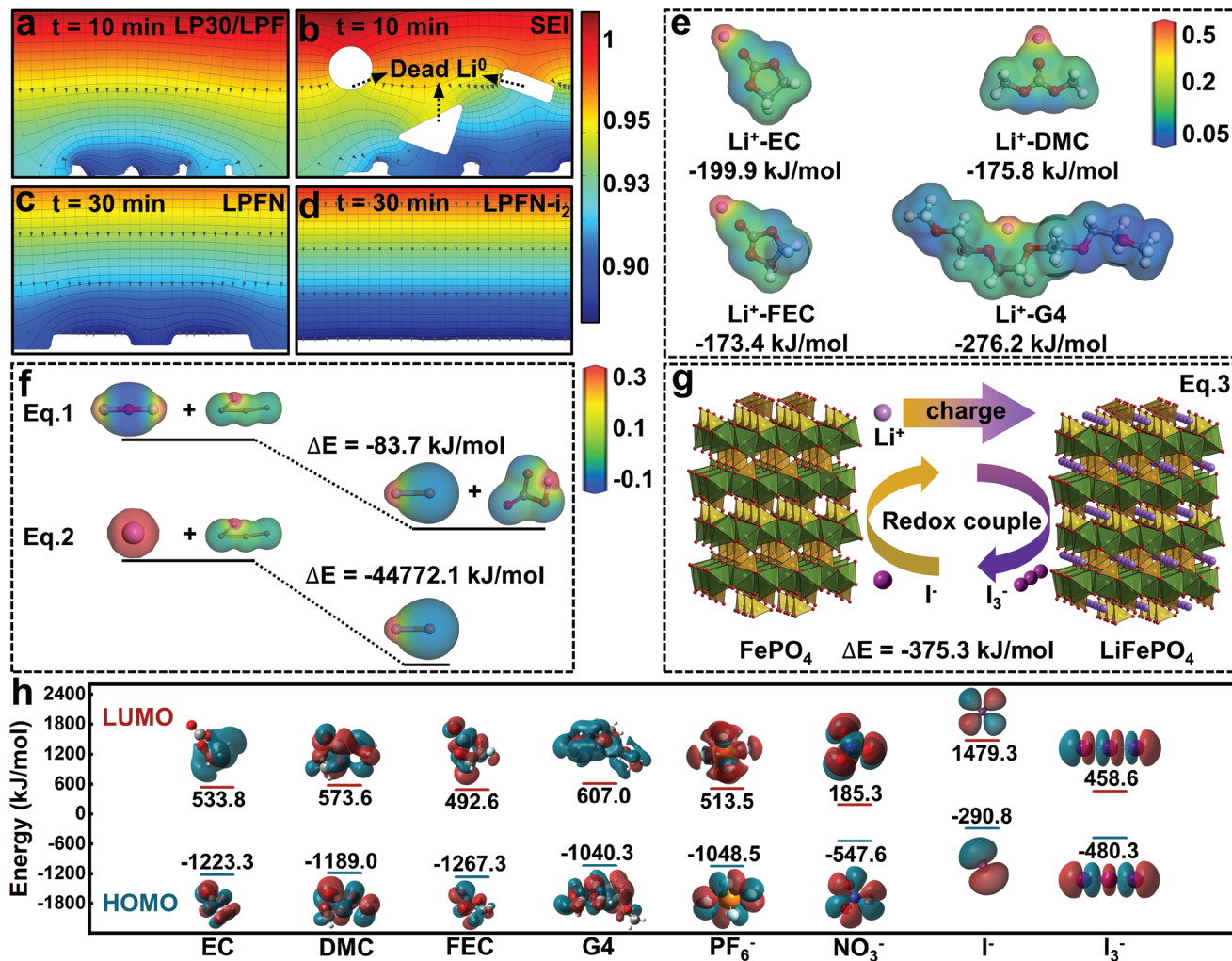


Figure 6. Simulation and theoretical calculation of various electrochemical behaviours. Finite element analysis of Li deposition behaviour simulated by COMSOL Multiphysics 5.6. Li deposition behaviour in a) LP30/LPF, c) LPFN, and d) LPFN-i₂ at current density of 0.5 mA cm⁻². b) The effect of dead Li⁰ in SEI on Li deposition behaviour. e) The binding energy and ESP of Li⁺-EC, Li⁺-DMC, Li⁺-FEC, and Li⁺-G4. The chemical mechanism of I₃⁻/I⁻ redox couple. f) The reaction energy ΔE of Equations (1) and (2). g) Schematic illustration of loss Li capacity regeneration and reaction energy ΔE of Equation (3) through I₃⁻/I⁻ redox couple. h) The LUMO and HOMO energy level of solvents and solutes using in our electrolytes.

with carbonate molecules and PF₆⁻ anion, NO₃⁻ has relatively lower LUMO energy level, namely stronger electron affinity, suggesting that NO₃⁻ will preferentially reduce to form Li₃N-rich and fast-ionic-conductivity SEI. And the LUMO energy level of FEC is lower than that of PF₆⁻ anion, which indicates LiF is mainly derived from the dedicated decomposition of FEC instead of PF₆⁻ anion. The atomic ratio obtained from in-depth XPS and EDX were carried out to support this assertion (see detail in Figure S37 in the Supporting Information). Moreover, I⁻ has highest HOMO energy level compared to other compositions, making the oxidation of I⁻ to I₃⁻ on the delithiated cathode side more advantageous and inhibiting the oxidation degradation of the solvent molecules to some extent. Likewise, I₃⁻ has the similar effect on the anode side due to the lower LUMO energy level than that of solvents.

Systematic investigations are conducted to evaluate the feasibility and effectiveness of the proposed electrolyte strategy in full cells. Compared to the rapid discharge capacity decay

in LP30 (41.6% capacity retention after 100 cycles) and LPF (75.5% capacity retention after 150 cycles), significantly enhanced reversibility and higher discharge capacity retention are obtained in LPFN (82.9% after 500 cycles) and LPFN-i₂ (88.4% after 500 cycles), preliminarily confirming the feasibility of HCA of LiNO₃ and I₃⁻/I⁻ redox couple in stabilizing Li anode interface and reclaiming irreversible inactive Li capacity (Figure 7a). Although the average CE (CE = discharge capacity/charge capacity) of LPFN-i₂ (99.5%) is slightly lower than that of LPFN (99.8%), much higher charge capacity can be also obtained in LPFN-i₂ accordingly due to capacity recovery effect (Figure S38, Supporting Information), which ensures the overall higher discharging capacity retention in LPFN-i₂ than LPFN. The capacity–voltage profiles with different cycles in LPFN-i₂ also demonstrate slow capacity decay even after a few hundred cycles (Figure 7b). Moreover, similar discharge capacity, much higher than that of LP30 and LPF, can be obtained in LPFN and LPFN-i₂ at 0.1, 0.5, 1, 2 C due to the lower interface resistance

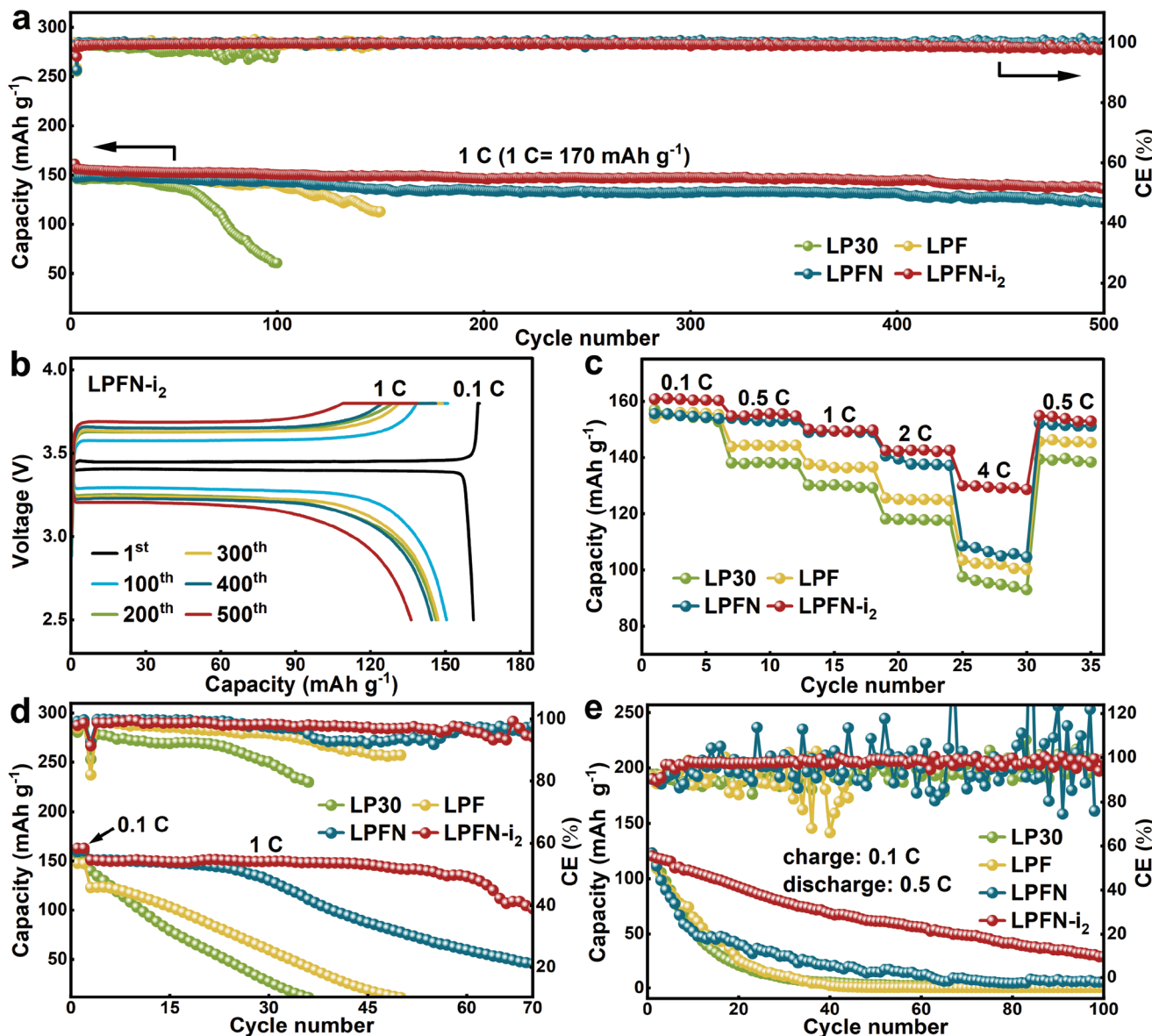


Figure 7. Electrochemical performance of the full cells with 12 mg cm^{-2} LiFePO₄ cathode in different electrolytes. a) Cycling performance of Li||LFPO cells at 1 C (1 C = 170 mAh g^{-1}). b) The charge–discharge curves of Li||LFPO in LPFN-i₂. c) Rate performance of Li||LFPO cells. d) Cycling performance of Li@Cu||LFPO with a limited Li capacity of 1.0 mAh cm^{-2} and an extremely low N/P ratio of 1.5 at 1 C. e) Cycling performance of Cu||LFPO cells charged at 0.1 C and discharged at 0.5 C.

with the addition of LiNO₃ (Figure 7c), as revealed by the EIS results (Figure S39, Supporting Information). However, when the rate is further increased up to 4 C, a remarkably improved rate capability emerges in LPFN-i₂ ($130.3 \text{ vs } 105.9, 100.5, 94.2 \text{ mAh g}^{-1}$), which may be attributed to more elastic and Li⁺-conducting oligomers induced by I₃⁻/I⁻ redox couple in the SEI. Excess Li used in anode tends to exaggerate electrochemical performance and even lead to misguided mechanism interpretation. Therefore, cells with extremely low negative to positive areal capacity ratio (N/P, 1.5) and anode-free lithium metal battery (AFLMB) are conducted to further evaluate the actual utility of I₃⁻/I⁻ redox couple in recovering inactive Li. 1.0 mAh cm^{-2} Li is predeposited on Cu current collector (denoted as Li@Cu)

and assemble the full cells against LFPO (Li@Cu||LFPO). Both LP30 and LPF exhibit plummeting capacity fade while LPFN only maintains relatively high capacity in the first 30 cycles (Figure 7d). However, slower capacity decay and higher capacity retention ($\approx 90.2\%$ after 60 cycles) can be obtained in LPFN-i₂. Moreover, AFLMB is employed with a critical protocol charging at small rate (0.1 C) and discharging at high rate (0.5 C), which has been proved to be beneficial for the stabilization of SEI in AFLMB.^[41] As shown in Figure 7e, the discharge capacity is almost lost after only 30 cycles for LP30, LPF, and LPFN while residual capacity ($\approx 30 \text{ mAh g}^{-1}$) is still preserved after even 100 cycles. Moreover, in contrast with the relatively stable CE (97.9% in 100 cycles) in LPFN-i₂, remarkable fluctuations appear

in the other three electrolytes, indicating the irrepressible side reaction in electrolytes without I_2 additive. Furthermore, inactive Li-covered cycled Li (obtained from $Li||Li$ symmetric cells at 3 mA cm^{-2} with fixed capacity of 3.0 mAh cm^{-2} after 200 cycles in LP30) and delithiated $LiFePO_4$ cathode were employed to assemble cells (Figure S40, Supporting Information). Different from the skimp capacity that is difficult to maintain normal operation in other electrolytes (LP30, LPF, and LPFN), the cycled $Li||$ delithiated $LiFePO_4$ cell can be successfully operated for 20 cycles with initial capacity of 74.0 mAh g^{-1} , which directly indicates the I_3^-/I^- redox couple can effectively convert the irreversible inactive Li into reversible capacity and restore them into delithiated cathode. Specially, according to previous study,^[25a] self-discharge problem will emerge with the introduction of I_3^-/I^- redox couple. Therefore, we also conducted experiments to detect the degree of self-discharge reaction in different electrolytes after standing 12, 24, and 48 h at 1 C ($1\text{ C} = 170\text{ mAh g}^{-1}$) in $Li||LiFePO_4$ cells. As shown in Figure S41a-d (Supporting Information), additive-free LP30 loses maximum discharge capacity ($\approx 14\text{ mAh g}^{-1}$) after standing 48 h while the capacity loss is suppressed to some extent in LPF ($\approx 7.3\text{ mAh g}^{-1}$ after 48 h) due to the passivation effect for Li anode by FEC. Compared to LP30 and LPF, almost negligible capacity decay ($\approx 1.0\text{ mAh g}^{-1}$ after standing 48 h) can be achieved in LPFN and LPFN-i₂, indicating the self-discharge is significantly inhibited due to the formation of efficient protective SEI layer. CV was conducted to detect the redox peaks of I_3^-/I^- redox couple in LPFN-i₂ electrolyte by $Li||NCM523$ cells between 2.8 and 4.3 V at 0.5 mV s^{-1} . As shown in Figure S41e-h (Supporting Information), the overall CV profiles of different electrolytes do not present distinct difference. However, clear redox peaks of I_3^-/I^- redox couple at around 3 V are observed in the enlarged view in LPFN-i₂, which indicates I_3^-/I^- redox couple can continuously regenerate at operating voltage over 3 V and contribute to the cell performance. Additionally, low-voltage cathode (LFPO) is replaced by high-voltage lithium–nickel–cobalt–manganese oxide (NCM523) to compare the high-voltage cycling performance of ether-containing carbonate-based electrolytes (LPFN and LPFN-i₂) with electrolytes containing only ester solvents (LP30 and LPF). Both LPFN and LPFN-i₂ outperform LP30 and LPF and higher capacity retention (93.3% in LPFN-i₂ and 84.7% in LPFN within 100 cycles) is achieved at 0.5 C ($1\text{ C} = 200\text{ mAh g}^{-1}$, Figure S42, Supporting Information), indicating the strategy of HCA can indeed function as a reliable strategy to improve high-voltage electrochemical performance of some Li-compatible solvents with low electrochemical oxidation windows.

3. Conclusion

In summary, we introduce HCA of $LiNO_3$ and I_3^-/I^- redox couple into carbonate-based electrolyte to construct an inorganic-rich SEI and rejuvenate the inactive Li, including the solvent/ $LiNO_3$ -derived Li_2O and electrically isolated dead Li^0 . HCA of $LiNO_3$ can not only avoid the disadvantages in (L)HCE (such as high viscosity, high cost) but also maintain its unique aggregated solvation structure that ensures a NO_3^- -derived SEI and significantly inhibits the oxidation of ether molecules at high

voltage. Moreover, the reversible I_3^-/I^- redox couple, unlike conventional sacrificial additives, can not only homogenize the SEI composition but also continuously convert the inactive (irreversible) Li capacity into delithiated cathode, leading to further improved cyclability and reversibility of LMBs. Consequently, a Li_3N -rich SEI with superior ionic conductivity and epitaxy-like planar Li deposition are achieved. Moreover, the feasibility of this strategy has been successfully verified through systematic investigations including $Li||Cu$ half cells, full cells with excess/limited Li capacity (N/P ratio = 1.5) and AFLMB and both observably enhanced reversibility and capacity retention are realized. This work provides a novel, promising and cost-effective additive strategy for prolonging the lifespan of LMBs in conventional carbonate-based electrolyte.

Supporting Information

Supporting Information is available from the Wiley Online Library or from the author.

Acknowledgements

The authors acknowledge the financial support by Natural Science Foundation for Distinguished Young Scholars of Hunan Province (2022JJ10089) and National Natural Science Foundation of China (52002405, U20A20123, 51874357), G.C. acknowledges the support from the 100 Talented program of Hunan Province and “Huxiang high-level talents” program (2019RS1007).

Conflict of Interest

The authors declare no conflict of interest.

Data Availability Statement

The data that support the findings of this study are available from the corresponding author upon reasonable request.

Keywords

high-concentration additives, inactive Li rejuvenation, lithium nitrate, redox couples

Received: April 27, 2022

Revised: June 1, 2022

Published online: June 22, 2022

- [1] Y. Zhang, T. Zuo, J. Popovic, K. Lim, Y. Yin, J. Maier, Y. Guo, *Mater. Today* **2019**, *33*, 56.
- [2] X. Cheng, R. Zhang, C. Zhao, Q. Zhang, *Chem. Rev.* **2017**, *117*, 10403.
- [3] S.-J. Tan, W.-P. Wang, Y.-F. Tian, S. Xin, Y.-G. Guo, *Adv. Funct. Mater.* **2021**, *31*, 2105253.
- [4] D. Lin, Y. Liu, Y. Cui, *Nat. Nanotechnol.* **2017**, *12*, 194.
- [5] C. Fang, J. Li, M. Zhang, Y. Zhang, F. Yang, J. Z. Lee, M.-H. Lee, J. Alvarado, M. A. Schroeder, Y. Yang, B. Lu, N. Williams, M. Ceja,

- L. Yang, M. Cai, J. Gu, K. Xu, X. Wang, Y. S. Meng, *Nature* **2019**, 572, 511.
- [6] a) C.-J. Huang, B. Thirumalraj, H.-C. Tao, K. N. Shitaw, H. Sutiono, T. T. Hagos, T. T. Beyene, L.-M. Kuo, C.-C. Wang, S.-H. Wu, W.-N. Su, B. J. Hwang, *Nat. Commun.* **2021**, 12, 1452; b) F. Liu, R. Xu, Y. Wu, D. T. Boyle, A. Yang, J. Xu, Y. Zhu, Y. Ye, Z. Yu, Z. Zhang, X. Xiao, W. Huang, H. Wang, H. Chen, Y. Cui, *Nature* **2021**, 600, 659; c) L. Hu, X. Zhang, P. Zhao, H. Fan, Z. Zhang, J. Deng, G. Ungar, J. Song, *Adv. Mater.* **2021**, 33, 2104416.
- [7] Z. Yu, H. Wang, X. Kong, W. Huang, Y. Tsao, D. G. Mackanic, K. Wang, X. Wang, W. Huang, S. Choudhury, Y. Zheng, C. V. Amanchukwu, S. T. Hung, Y. Ma, E. G. Lomeli, J. Qin, Y. Cui, Z. Bao, *Nat. Energy* **2020**, 5, 526.
- [8] H. Zhang, X. Liao, Y. Guan, Y. Xiang, M. Li, W. Zhang, X. Zhu, H. Ming, L. Lu, J. Qiu, Y. Huang, G. Cao, Y. Yang, L. Mai, Y. Zhao, H. Zhang, *Nat. Commun.* **2018**, 9, 3729.
- [9] X. Gao, Y.-N. Zhou, D. Han, J. Zhou, D. Zhou, W. Tang, J. B. Goodenough, *Joule* **2020**, 4, 1864.
- [10] a) Z. Wen, W. Fang, L. Chen, Z. Guo, N. Zhang, X. Liu, G. Chen, *Adv. Funct. Mater.* **2021**, 31, 2104930; b) K. Kim, H. Ma, S. Park, N.-S. Choi, *ACS Energy Lett.* **2020**, 5, 1537.
- [11] a) N. Piao, S. Liu, B. Zhang, X. Ji, X. Fan, L. Wang, P.-F. Wang, T. Jin, S.-C. Liou, H. Yang, J. Jiang, K. Xu, M. A. Schroeder, X. He, C. Wang, *ACS Energy Lett.* **2021**, 6, 1839; b) K. Xu, *Chem. Rev.* **2004**, 104, 4303; c) X. Fan, C. Wang, *Chem. Soc. Rev.* **2021**, 50, 10486.
- [12] a) S. Zhang, G. Yang, Z. Liu, X. Li, X. Wang, R. Chen, F. Wu, Z. Wang, L. Chen, *Nano Lett.* **2021**, 21, 3310; b) X. Wang, S. Wang, H. Wang, W. Tu, Y. Zhao, S. Li, Q. Liu, J. Wu, Y. Fu, C. Han, F. Kang, B. Li, *Adv. Mater.* **2021**, 33, 2007945; c) X.-Q. Zhang, X. Chen, X.-B. Cheng, B.-Q. Li, X. Shen, C. Yan, J.-Q. Huang, Q. Zhang, *Angew. Chem., Int. Ed.* **2018**, 57, 5301.
- [13] S. Liu, X. Ji, N. Piao, J. Chen, N. Eidson, J. Xu, P. Wang, L. Chen, J. Zhang, T. Deng, S. Hou, T. Jin, H. Wan, J. Li, J. Tu, C. Wang, *Angew. Chem., Int. Ed.* **2021**, 60, 3661.
- [14] Y. Jie, X. Liu, Z. Lei, S. Wang, Y. Chen, F. Huang, R. Cao, G. Zhang, S. Jiao, *Angew. Chem., Int. Ed.* **2020**, 59, 3505.
- [15] S. Li, W. Zhang, Q. Wu, L. Fan, X. Wang, X. Wang, Z. Shen, Y. He, Y. Lu, *Angew. Chem., Int. Ed.* **2020**, 59, 14935.
- [16] C. Yan, Y.-X. Yao, X. Chen, X.-B. Cheng, X.-Q. Zhang, J.-Q. Huang, Q. Zhang, *Angew. Chem., Int. Ed.* **2018**, 57, 14055.
- [17] W. Zhang, Q. Wu, J. Huang, L. Fan, Z. Shen, Y. He, Q. Feng, G. Zhu, Y. Lu, *Adv. Mater.* **2020**, 32, 2001740.
- [18] X. Wang, S. Li, W. Zhang, D. Wang, Z. Shen, J. Zheng, H. L. Zhuang, Y. He, Y. Lu, *Nano Energy* **2021**, 89, 106353.
- [19] R. Xu, X. Shen, X.-X. Ma, C. Yan, X.-Q. Zhang, X. Chen, J.-F. Ding, J.-Q. Huang, *Angew. Chem., Int. Ed.* **2020**, 60, 4215.
- [20] L. Li, H. Dai, C. Wang, *Nano Select* **2021**, 2, 16.
- [21] X. Cao, H. Jia, W. Xu, J.-G. Zhang, *J. Electrochem. Soc.* **2021**, 168, 010522.
- [22] a) K. Yoshida, M. Nakamura, Y. Kazue, N. Tachikawa, S. Tsuzuki, S. Seki, K. Dokko, M. Watanabe, *J. Am. Chem. Soc.* **2011**, 133, 13121; b) D. Xiao, Q. Li, D. Luo, G. Li, H. Liu, L. Shui, S. Gourley, G. Zhou, X. Wang, Z. Chen, *Small* **2020**, 16, 2004688.
- [23] X. Xin, K. Ito, A. Dutta, Y. Kubo, *Angew. Chem., Int. Ed.* **2018**, 57, 13206.
- [24] C. Jin, T. Liu, O. Sheng, M. Li, T. Liu, Y. Yuan, J. Nai, Z. Ju, W. Zhang, Y. Liu, Y. Wang, Z. Lin, J. Lu, X. Tao, *Nat. Energy* **2021**, 6, 378.
- [25] a) Q. Zhao, Y. Lu, Z. Zhu, Z. Tao, J. Chen, *Nano Lett.* **2015**, 15, 5982; b) Y. Zhao, L. Wang, H. R. Byon, *Nat. Commun.* **2013**, 4, 1896.
- [26] C.-B. Jin, X.-Q. Zhang, O.-W. Sheng, S.-Y. Sun, L.-P. Hou, P. Shi, B.-Q. Li, J.-Q. Huang, X.-Y. Tao, Q. Zhang, *Angew. Chem., Int. Ed.* **2021**, 60, 22990.
- [27] W. Wahyudi, V. Ladelta, L. Tsetseris, M. M. Alsabban, X. Guo, E. Yengel, H. Faber, B. Adilbekova, A. Seitkhan, A.-H. Emwas, M. N. Hedhili, L.-J. Li, V. Tung, N. Hadjichristidis, T. D. Anthopoulos, J. Ming, *Adv. Funct. Mater.* **2021**, 31, 2101593.
- [28] J. Fawdon, J. Ihli, F. L. Mantia, M. Pasta, *Nat. Commun.* **2021**, 12, 4053.
- [29] C.-C. Su, M. He, J. Shi, R. Amine, J. Zhang, K. Amine, *Angew. Chem., Int. Ed.* **2020**, 59, 18229.
- [30] C. Ling, R. Zhang, K. Takechi, F. Mizuno, *J. Phys. Chem. C* **2014**, 118, 26591.
- [31] T. Li, X.-Q. Zhang, P. Shi, Q. Zhang, *Joule* **2019**, 3, 2647.
- [32] J. Tan, J. Matz, P. Dong, J. Shen, M. Ye, *Adv. Energy Mater.* **2021**, 11, 2100046.
- [33] N. Tapia-Ruiz, A. G. Gordon, C. M. Jewell, H. K. Edwards, C. W. Dunnill, J. M. Blackman, C. P. Snape, P. D. Brown, I. MacLaren, M. Baldoni, E. Besley, J. J. Titman, D. H. Gregory, *Nat. Commun.* **2020**, 11, 4492.
- [34] X. Fan, X. Ji, F. Han, J. Yue, J. Chen, L. Chen, T. Deng, J. Jiang, C. Wang, *Sci. Adv.* **2018**, 4, eaau9245.
- [35] Y. Wang, F. Liu, G. Fan, X. Qiu, J. Liu, Z. Yan, K. Zhang, F. Cheng, J. Chen, *J. Am. Chem. Soc.* **2021**, 143, 2829.
- [36] F. Wu, J. T. Lee, N. Nitta, H. Kim, O. Borodin, G. Yushin, *Adv. Mater.* **2015**, 27, 101.
- [37] R. Guo, B. M. Gallant, *Chem. Mater.* **2020**, 32, 5525.
- [38] M. Tułodziecki, G. M. Leverick, C. V. Amanchukwu, Y. Katayama, D. G. Kwabi, F. Bardé, P. T. Hammond, Y. Shao-Horn, *Energy Environ. Sci.* **2017**, 10, 1828.
- [39] G. M. Hobold, J. Lopez, R. Guo, N. Minafra, A. Banerjee, Y. Shirley Meng, Y. Shao-Horn, B. M. Gallant, *Nat. Energy* **2021**, 6, 951.
- [40] W. Tang, X. Yin, Z. Chen, W. Fu, K. P. Loh, G. W. Zheng, *Energy Storage Mater.* **2018**, 14, 289.
- [41] M. Genovese, A. J. Louli, R. Weber, S. Hames, J. R. Dahn, *J. Electrochem. Soc.* **2018**, 165, A3321.